Fully kinetic simulation of ion-temperature-gradient instabilities in tokamaks

by Youjun Hu[1,2], Matthew T. Miecnikowski[1], Yang Chen[1], Scott E. Parker[1]

1. Department of Physics, University of Colorado, Boulder, CO 80309, USA
2. Institute of Plasma Physics, Chinese Academy of Sciences, Hefei 230031, China
Email: youjun.hu@colorado.edu (Youjun Hu)

Abstract

The feasibility of using full ion kinetics, instead of gyrokinetics, in simulating low-frequency Ion-Temperature-Gradient (ITG) instabilities in tokamaks has recently been demonstrated by Sturdevant et al. [*Physics of Plasmas* **24**, 081207 (2017)]. The present work extends that work to the nonlinear regime and investigates the nonlinear saturation of a single-n ITG instability due to the $E \times B$ trapping mechanism (n is the toroidal mode number). The saturation amplitude predicted by the $E \times B$ trapping theory is found to agree with the saturation level observed in the simulation. In extending to the nonlinear regime, we developed a toroidal Boris full orbit integrator, which proved to be accurate in capturing both the short-time scale cyclotron motion and long time scale drift motion, with good kinetic energy conservation and toroidal angular momentum conservation in tokamak equilibrium magnetic fields. This work also extends the previous work from analytic circular magnetic equilibria to general numerical magnetic equilibria, enabling simulation of realistic equilibria reconstructed from tokamak experiments.

1 Introduction

Ion temperature gradients in tokamaks provide free energy to micro-instabilities called Ion-Temperature-Gradient (ITG) instabilities[1]. The nonlinear development of these instabilities, i.e., ITG turbulence, is believed to play an important role in regulating particle and heat transport in tokamaks[2, 3, 4]. There are numerous papers devoted to the gyrokinetic simulation of ITG turbulence, which employ gyrokinetic theory to decouple the high-frequency gyro-motion of ions from the low-frequency ITG modes[5, 6, 7, 8, 9, 10]. However, gyrokinetics rely on ordering assumptions in deriving the gyrokinetic equation. One of these ordering assumptions, $\rho_i/L_n \ll 1$, becomes questionable in tokamak edge with steep density profile, where ρ_i is the gyro-radius of ions and L_n is the scale length of density profile. For this reason, tokamak edge gyrokinetic codes, e.g. XGC[11, 12], are usually limited in the regime where the pedestal width is much greater than the ion gyro-radius. Fully kinetic ion models[13, 14, 15, 16, 17], which retain the ion gyro-motion, avoid these problematic ordering assumptions (although involving more computations in simulations). Low-frequency full kinetics have already been demonstrated in slab geometry[18], successfully benchmarked against gyrokinetics for the slab ITG[19], and extended to toroidal ITG instabilities by Sturdevant et al.[20].

The present work extend that of Ref. [20] to the nonlinear regime and investigates the nonlinear saturation of a single-n ITG instability due to the $E \times B$ trapping mechanism (n is the toroidal mode number). The saturation amplitude predicted by the $E \times B$ trapping theory is found to agree with the saturation level observed in the simulation. In extending to the nonlinear regime, we developed a toroidal Boris full orbit integrator, which proved to be accurate in capturing both the short-time scale cyclotron motion and long time scale drift motion, with good kinetic energy conservation and toroidal angular momentum conservation in tokamak equilibrium magnetic fields. This work also extends the previous work from analytic circular magnetic equilibria to general numerical magnetic equilibria, enabling simulation of realistic equilibria reconstructed from tokamak experiments.

To verify the new numerical implementation of the orbit integrator and magnetic configuration, the linear electrostatic ITG frequency and growth rate are compared with the fully kinetic results of Ref. [20] and gyrokinetic results of Ref. [22]. Good agreement is found for both cases. Our simulation adopts the δf particle-in-cell (PIC) method.

The remainder of the paper is organized as follows. Section 2 discusses the fully kinetic ion model for simulating ITG instabilities. The implicit δf PIC method and the full orbit integrator are briefly discussed in Sec. 3. Section 4 discusses how magnetic configuration and magnetic coordinates are handled in our numerical model. Section 5 gives the linear and nonlinear results of ITG instabilities, along with a benchmark against the fully kinetic results of Ref. [20] and gyrokinetic results of Ref. [22] in the linear regime. A brief

summary is given in Sec. 6.

2　Fully kinetic ion model of ITG instabilities

The fully kinetic ion model for ITG instabilities is described in Ref. [20]. The following is a summary of the model. The ion Vlasov equation is written

$$\frac{df_i}{dt} \equiv \frac{\partial f_i}{\partial t} + \mathbf{v} \cdot \frac{\partial f_i}{\partial \mathbf{x}} + \frac{q_i}{m_i}(\mathbf{E} + \mathbf{v} \times \mathbf{B}) \cdot \frac{\partial f_i}{\partial \mathbf{v}} = 0, \tag{1}$$

where $f_i(\mathbf{x}, \mathbf{v})$ is the ion distribution function, $\mathbf{x}$ and $\mathbf{v}$ are ion position and velocity respectively, $\mathbf{E}$ and $\mathbf{B}$ are the electric field and magnetic field respectively, q_i and m_i are the charge and mass of ions respectively. We write f_i as an equilibrium part plus a perturbation, i.e., $f_i = f_{i0} + \delta f_i$, then Eq. (1) is written as

$$\frac{d\delta f_i}{dt} = -\frac{q_i}{m_i}(\delta \mathbf{E} + \mathbf{v} \times \delta \mathbf{B}) \cdot \frac{\partial f_{i0}}{\partial \mathbf{v}}, \tag{2}$$

where $\delta \mathbf{E}$ and $\delta \mathbf{B}$ are the perturbed part of the electric field and magnetic field, respectively.

To model ITG instabilities, the equilibrium part of ion distribution function f_{i0} is chosen as[20]

$$f_{i0}(R_r, v) = n_{i0}(R_r)\left(\frac{m_i}{2\pi T_{i0}(R_r)}\right)^{3/2} \exp\left[-\frac{m_i v^2}{2T_{i0}(R_r)}\right], \tag{3}$$

where n_{i0} and T_{i0} are ion number density and temperature, which depend on a radial variable R_r given by

$$R_r = r + \frac{m_i}{q_i}\frac{\mathbf{v} \times \mathbf{b}}{B_0} \cdot \nabla r, \tag{4}$$

where r is the minor radius of magnetic surfaces and $\mathbf{b} = \mathbf{B}_0 / B_0$ is the unit vector along the equilibrium magnetic field $\mathbf{B}_0$. The variable R_r is a radial coordinate of the ion guiding-center and thus an approximate constant of motion in the weakly inhomogeneous tokamak magnetic field with $\rho_i / L_B \ll 1$, where L_B is the scale length of $\mathbf{B}_0$. Since arbitrary functions of the constants of motion are solutions to the kinetic equation, the distribution function given by Eq. (3) is approximately an equilibrium solution to the kinetic equation (1). Using this form of equilibrium distribution, the kinetic equation (2) for the perturbed part of the distribution is written as

$$\begin{aligned}
\frac{d\delta f_i}{dt} &= \frac{q_i}{T_i}f_{i0}\delta \mathbf{E} \cdot \mathbf{v} + \left[\kappa_{n_i} + \left(\frac{mv^2}{2T_i} - \frac{3}{2}\right)\kappa_{T_i}\right]f_{i0}\frac{(\delta \mathbf{E} \times \mathbf{b}) \cdot \nabla r}{B_0} \\
&\quad - \left[\kappa_{n_i} + \left(\frac{mv^2}{2T_i} - \frac{3}{2}\right)\kappa_{T_i}\right]f_{i0}(\mathbf{v} \times \delta \mathbf{B}) \cdot \frac{\nabla r \times \mathbf{b}}{B_0},
\end{aligned} \tag{5}$$

where $\kappa_{n_i} = -n_{i0}^{-1}\partial n_{i0}/\partial R_r$ and $\kappa_{T_i} = -T_{i0}^{-1}\partial T_{i0}/\partial R_r$ are the radial gradients of ion density and temperature, respectively.

2.1　Electrostatic limit with adiabatic electrons

In this work, we focus on the electrostatic limit, in which $\delta \mathbf{B}$ is zero and $\delta \mathbf{E} = -\nabla \delta \Phi$, where $\delta \Phi$ is the perturbed electric potential. Furthermore, we adopt the simple adiabatic electron model for describing the electron response, in which the perturbed electron density is related to $\delta \Phi$ by

$$\delta n_e = n_{e0}\frac{e(\delta \Phi - \langle \delta \Phi \rangle)}{T_{e0}}, \tag{6}$$

where n_{e0} and T_{e0} are the equilibrium electron number density and temperature, respectively; e is the elementary charge, $\langle ... \rangle$ is the magnetic surface averaging operator defined by

$$\langle ... \rangle = \frac{\int_0^{2\pi}\int_{-\pi}^{+\pi}(...)\mathcal{J}d\phi d\theta}{\int_0^{2\pi}\int_{-\pi}^{+\pi}\mathcal{J}d\phi d\theta}, \tag{7}$$

where $\mathcal{J} = \mathcal{J}(\psi, \theta)$ is the Jacobian of magnetic coordinates (ψ, θ, ϕ), ψ is a radial coordinate, θ and ϕ are poloidal and toroidal angles, respectively.

In the electrostatic limit, Maxwell's equations reduce to Poisson's equation, which further reduces to the

quasi-neutrality condition if the space-charge term is neglected. The quasi-neutrality condition is written as

$$\delta n_e = \delta n_i \tag{8}$$

where δn_i is the perturbed part of the ion number density. Using δn_e given by Eq. (6) in the above equation, we obtain

$$n_{e0}\frac{e(\delta\Phi - \langle\delta\Phi\rangle)}{T_e} = \delta n_i, \tag{9}$$

which serves as our field equation, from which the electric potential $\delta\Phi$ can be solved. We consider modes with $n \neq 0$, where n is the toroidal mode number. Then the flux average $\langle\delta\Phi\rangle$ is always zero and the field equation (9) reduces to an algebraic equation, which can be analytically solved to give

$$\delta\Phi = \frac{T_e}{e}\frac{\delta n_i}{n_{e0}}. \tag{10}$$

3 Implicit δf particle-in-cell method and full orbit integrator

The ion Vlasov equation (5) is solved by using the δf PIC method[24, 25], in which an assembly of markers are loaded in the phase-space according to a distribution function $g(\mathbf{x}, \mathbf{v})$. Then the phase space volume sampled by a marker located at $(\mathbf{x}_j, \mathbf{v}_j)$ is given by $V_{\text{ps }j} = 1/g(\mathbf{x}_j, \mathbf{v}_j)$. We define the weight of the jth marker by

$$w_{ij} = \delta f_i(\mathbf{x}_j, \mathbf{v}_j)V_{\text{ps }j} = \frac{\delta f_i(\mathbf{x}_j, \mathbf{v}_j)}{g(\mathbf{x}_j, \mathbf{v}_j)}, \tag{11}$$

which is the physical particle number carried by δf_i in the phase space volume $V_{\text{ps }j}$. The weight evolution equation is obtained by multiplying both sides of Eq. (5) by $V_{\text{ps }j}$ and noting that $d(V_{\text{ps }j})/dt = 0$, yielding

$$
\begin{aligned}
\frac{dw_{ij}}{dt} &= \frac{f_{i0}}{g}\frac{q_i}{T_i}\delta\mathbf{E}\cdot\mathbf{v} \\
&+ \frac{f_{i0}}{g}\left[\kappa_{n_i} + \left(\frac{mv^2}{2T_i} - \frac{3}{2}\right)\kappa_{T_i}\right]\frac{(\delta\mathbf{E}\times\mathbf{b})\cdot\nabla r}{B_0},
\end{aligned}
\tag{12}
$$

where the magnetic perturbation terms have been dropped due to the electrostatic approximation. An implicit scheme is used to integrate the weight evolution equation. Denoting the right-hand side of the weight evolution equation (12) by $h(\delta\mathbf{E}, \mathbf{x}, \mathbf{v})$, the implicit scheme we use takes the following form:

$$\frac{w_{ij}^{(n+1)} - w_{ij}^{(n)}}{\Delta t} = h\left(\delta\mathbf{E}^{(n+1/2)}, \mathbf{x}_j^{(n+1/2)}, \mathbf{v}_j^{(n+1/2)}\right), \tag{13}$$

with

$$\delta\mathbf{E}^{(n+1/2)} = \frac{\delta\mathbf{E}^{(n+1)} + \delta\mathbf{E}^{(n)}}{2}, \tag{14}$$

where the super-indexes n and $n+1$ indicate current and future time step, respectively. We choose the initial guess of $\delta\mathbf{E}^{(n+1)}$ to be equal to $\delta\mathbf{E}^{(n)}$ and then iterate until convergence is achieved. If the iteration is terminated after only two iterations, then this scheme corresponds to the predictor-corrector scheme called Heun's method[26]. The field equation (9) needs to be solved once at t_{n+1} to obtain $\delta\mathbf{E}^{(n+1)}$ in each iteration.

The ion trajectory $(\mathbf{x}_j, \mathbf{v}_j)$ is advanced by a time-centered difference scheme given by

$$\frac{\mathbf{v}^{(n+1/2)} - \mathbf{v}^{(n-1/2)}}{\Delta t} = \frac{q_i}{m_i}\left[\mathbf{E}^{(n)}(\mathbf{x}^{(n)}) + \frac{\mathbf{v}^{(n+1/2)} + \mathbf{v}^{(n-1/2)}}{2}\times\mathbf{B}^{(n)}(\mathbf{x}^{(n)})\right]. \tag{15}$$

for velocity and

$$\frac{\mathbf{x}^{(n+1)} - \mathbf{x}^{(n)}}{\Delta t} = \mathbf{v}^{(n+1/2)}, \tag{16}$$

for position. Here "staggered" time grids are used for $\mathbf{v}$ and $\mathbf{x}$: time grids of $\mathbf{v}$ are at half-steps while time grids of $\mathbf{x}$ are at integer steps. The position at half-steps, $\mathbf{x}^{(n+1/2)}$, which is needed in Eq. (13), is approximated by $\mathbf{x}^{(n+1/2)} = (\mathbf{x}^{(n)} + \mathbf{x}^{(n+1)})/2$. Further note that the scheme given in Eq (15) is in an implicit form since the unknown $\mathbf{v}^{(n+1/2)}$ appears on both sides of the equation. Fortunately, equation (15) can be analytically solved in Cartesian basis and its explicit solution is expressed by the Boris algorithm[23]. As is discussed

in Ref. [27], the above scheme conserves the phase-space volume, which makes it suitable for particle-based methods where phase-space volume conservation is usually implicitly assumed. In this work, cylindrical coordinates are used in integrating the ion orbits. When implementing the Boris scheme in cylindrical coordinates, a local Cartesian coordinate system with basis vectors $(\mathbf{e}_x, \mathbf{e}_y, \mathbf{e}_z)$ along the local cylindrical basis vectors $(\mathbf{e}_R, \mathbf{e}_\phi, \mathbf{e}_Z)$ at particle location $\mathbf{x}^{(n)}$ is set up to perform the velocity integration to obtain $\mathbf{v}^{(n+1/2)}$. Then the particle location is updated in the local Cartesian coordinates by using Eq. (16) and then is transformed to the cylindrical coordinates by using the analytic coordinate transformation. After this, the new velocity $\mathbf{v}^{(n+1/2)}$ is projected onto the new basis vectors $(\mathbf{e}_R, \mathbf{e}_\phi, \mathbf{e}_Z)$ at particle location $\mathbf{x}^{(n+1)}$. Typical full ion orbits computed by this scheme are compared with the guiding center orbit in Figure 1. This scheme can reproduce correct drift motion even when a large time-step comparable to the gyro-period is used[28]. Figure 1 shows examples of orbits computed with large time steps.
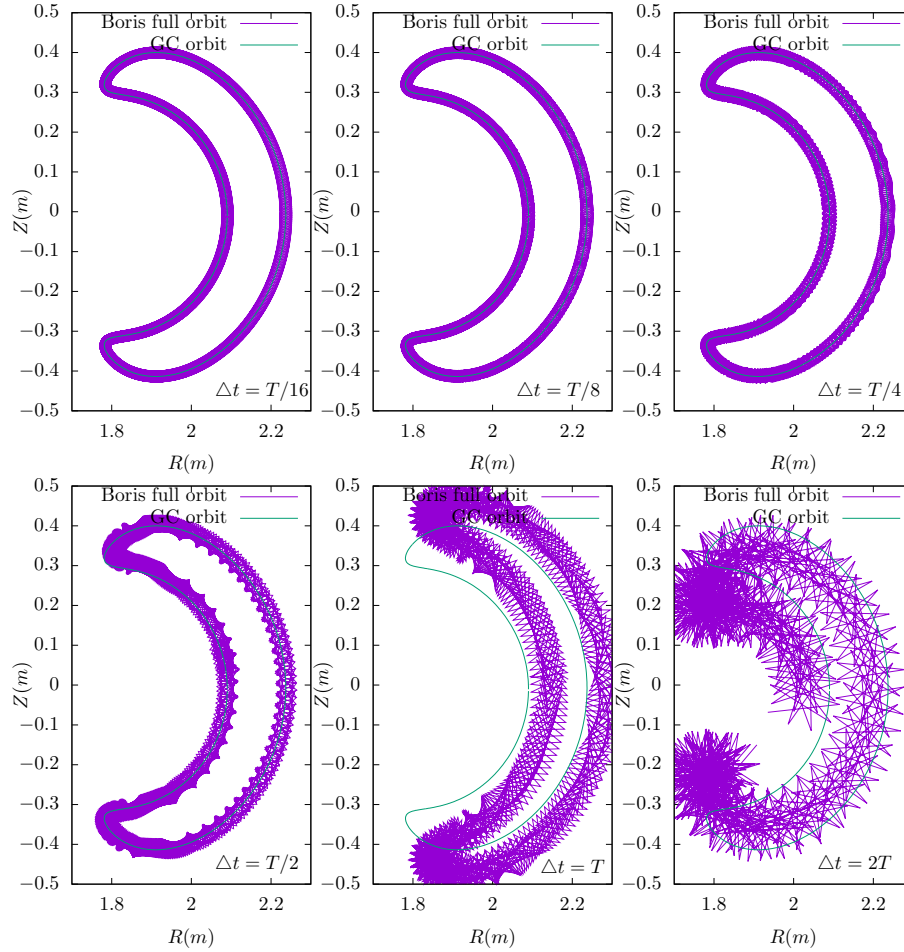

Figure 1. Comparison between the full orbits calculated by the Boris scheme with different time step sizes: $\Delta t = T/16$, $\Delta t = T/8$, $\Delta t = T/4$, $\Delta t = T/2$, $\Delta t = T$, and $\Delta t = 2T$, where T is the ion (Deuteron) gyro-period at its initial location $(R = 2.1m, Z = 0m, \phi = 0)$. The results show that the full orbits agrees with the guiding-center orbit for the cases with time-step $\Delta t < T/4$. When Δt is further increased, the computed full orbits deviate from the guiding-center orbit. Further note that the gyro-radius obtained remains nearly the same when the time-step $\Delta t < T/4$. When Δt is further increased, the gyro-radius becomes larger than the correct value. The magnetic configuration is from EAST tokamak discharge#59954@3.03s. The initial velocity is given by $v_R = v_Z = 1.0 \times 10^6 m/s$, and $v_\phi = 5 \times 10^5 m/s$, where (v_R, v_ϕ, v_Z) are the velocity components in the cylindrical coordinate system. This corresponds to a kinetic energy of 23keV. For $\Delta t = T/16$, the orbit is advanced by 23250 time-steps, in which the particle finishes one banana period.

Figure 2 plots the relative variation of the kinetic energy E_k and toroidal angular momentum P_ϕ computed by the Boris full orbit integrator over a time period of $t\Omega_i = 2.5 \times 10^4$ for different time step sizes in a tokamak equilibrium magnetic field, where Ω_i is the ion cyclotron angular frequency at the magnetic axis.

The results indicate that the kinetic energy conservation is accurate to the machine error and the relative error in the toroidal angular momentum conservation is within 0.04%. The kinetic energy conservation of the Boris integrator is much better than the variational integrator of Ref. [20]. This is because the Boris integrator directly rotates the velocity, which does not change the amplitude of the velocity when no electric field is present.
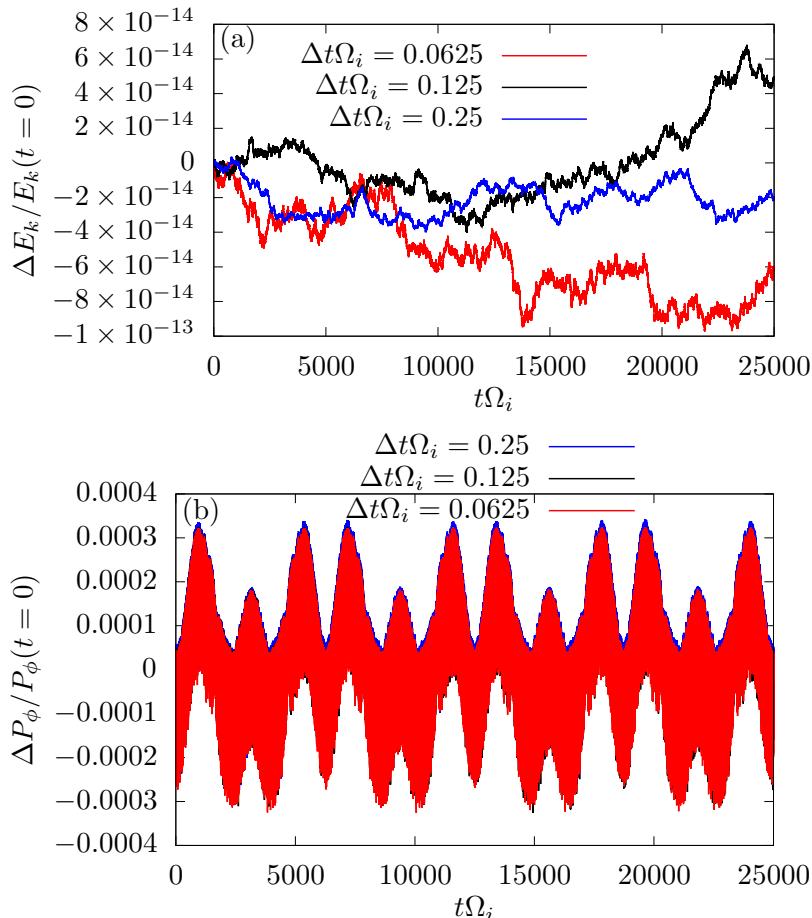

Figure 2. The relative variation of the kinetic energy (a) and toroidal angular momentum (b) given by the Boris full orbit integrator over a time period of $t\Omega_i = 2.5 \times 10^4$ for different time step sizes in a tokamak equilibrium magnetic field. The initial conditions of the orbit are $R = 1.176R_0$, $Z = 3.912 \times 10^{-3}R_0$, $v_R = 3.371 \times 10^{-3}R_0\Omega_i$, $v_Z = 3.371 \times 10^{-3}R_0\Omega_i$, and $v_\phi = -1.798 \times 10^{-3}R_0\Omega_i$, where $R_0 = 1.32m$ and the magnetic configuration is the DIII-D cyclone base case, which is specified in Table 1. The toroidal angular momentum is defined by $P_\phi = m_i R v_\phi + q_i \Psi$, where Ψ is the poloidal magnetic flux function.

In the linear limit, the fields $\mathbf{E}$ and $\mathbf{B}$ on the right-hand side of Eq (15) are replaced by the equilibrium fields $\mathbf{E}_0$ and $\mathbf{B}_0$. In the present work, $\mathbf{E}_0 = 0$ and $\mathbf{B}_0$ is a general toroidal magnetic configuration specified numerically.

4 Magnetic field specification and field-line-following coordinates

The equilibrium magnetic field is specified numerically by reading and interpolating the output of the equilibrium reconstruction code EFIT[29]. This enables us to handle magnetic configurations with arbitrary flux surface shape.

A field-line-following coordinate system[30, 31] (ψ, θ, α) is constructed from the numerical magnetic configuration, with the radial coordinate ψ being the normalized poloidal magnetic flux, θ being an equal-volume poloidal angle and α being a generalized toroidal angle defined by $\alpha = \phi - \int_0^\theta \hat{q} d\theta$, where ϕ is the

cylindrical toroidal angle, and $\hat{q} = \mathbf{B} \cdot \nabla \phi / \mathbf{B} \cdot \nabla \theta$ is the local safety factor. In (ψ, θ, α) coordinate system, both $\nabla \psi$ and $\nabla \alpha$ are perpendicular the field lines, i.e. $\mathbf{B}_0 \cdot \nabla \psi = 0$, and $\mathbf{B}_0 \cdot \nabla \alpha = 0$. Furthermore the gradient along the field line is written as

$$\mathbf{B}_0 \cdot \nabla = -\Psi' \mathcal{J}^{-1} \frac{\partial}{\partial \theta}, \tag{17}$$

where $\Psi' = d\Psi / d\psi$ with $\Psi = A_\phi R$ the poloidal magnetic flux function, and $\mathcal{J} = (\nabla \psi \times \nabla \theta \cdot \nabla \alpha)^{-1}$ is the Jacobian of the (ψ, θ, α) coordinates.

Ion markers are loaded in the field-line-following coordinates (ψ, θ, α). Ion trajectories are integrated in cylindrical coordinates (R, ϕ, Z) and then linearly interpolated to (ψ, θ, α) coordinates to do the deposition in order to obtain the perturbed ion density at the spatial grids of (ψ, θ, α) coordinates. At a grid point $\mathbf{x}_k$, the perturbed ion density is approximated by

$$\delta n_i(\mathbf{x}_k) = \frac{1}{\Delta V_s} \sum_{j=1}^{N_p} w_{ij} S(\mathbf{x}_k - \mathbf{x}_j), \tag{18}$$

where N_p is the total number of markers loaded, $\Delta V_s = \mathcal{J}(\mathbf{x}_k) \Delta \psi \Delta \theta \Delta \alpha$ is the volume of the spatial cell, $\Delta \psi$, $\Delta \theta$, and $\Delta \alpha$ are the grid point spacings in the ψ, θ and α direction respectively, S is the interpolating function defined as

$$S(\mathbf{x}) = S_{1D}\left(\frac{\psi}{\Delta \psi}\right) S_{1D}\left(\frac{\theta}{\Delta \theta}\right) S_{1D}\left(\frac{\alpha}{\Delta \alpha}\right), \tag{19}$$

with S_{1D} being the first-order b-spline function given by

$$S_{1D}(x) = \begin{cases} 1 - |x| & : |x| \leqslant 1 \\ 0 & : |x| > 1 \end{cases}, \tag{20}$$

(then the deposition corresponds to a linear interpolation). In this work, the marker distribution function g is chosen as $g = f_{i0} N_p / (V_s n_{i0})$, where V_s the spatial volume of the computational box.

After solving the field equation for $\delta \Phi$, the spatial differential of $\delta \Phi$ is performed in the field-line-following coordinates to determine the perturbed electric field. The deposition and field solving are done in field-line-following coordinates because this coordinate system is efficient for resolving ITG modes, which have $k_\parallel \ll k_\perp$, where $k_\parallel$ and $k_\perp$ are the parallel and perpendicular wave-number, respectively.

5 Simulation results of ITG instabilities

In order to benchmark the results against those of Ref. [20], we adopt the DIII-D cyclone base case[21], which is a concentric-circular magnetic configuration. The main parameters used in the benchmarking are summarized in Table. 1.

R_0	a	B_{axis}	q_0	$\hat{s}$	r_0	$\kappa_{T_i} R_0$	$\kappa_{n_i} R_0$	T_{i0}	$q_i T_{i0} / (e T_{e0})$
$1.32m$	$0.48m$	$1.91T$	1.40	0.78	$0.24m$	6.9	2.2	1.5keV	1

Table 1. DIII-D cyclone base case parameters[21]. The safety factor profile is given by $q(r) = q_0 + (r - r_0)q'(r_0)$ with $q'(r_0) = \hat{s} q_0 / r_0$, where $\hat{s}$ is the magnetic shear at $r = r_0$ (the radial center of the simulation box). In this case $R_0 / \rho_i = 450.5$, where $\rho_i = v_{ti} / \Omega_i$ is the thermal ion gyro-radius at the magnetic axis, $v_{ti} = \sqrt{T_{i0}/m_i}$, $\Omega_i = B_{\text{axis}} q_i / m_i$ is the ion cyclotron angular frequency at the magnetic axis. Deuterium plasma is assumed in our simulation.

Although the DIII-D cyclone equilibrium is analytic and circular, the equilibrium is read in as a general equilibrium specified numerically in the G-EQDSK format of EFIT code. No analytic relations particular to this specific configuration is relied on.

The radial center of the simulation box is at $r = r_0 = 0.24m$ and the radial width $\Delta r = 0.11m$, which is about $37.5\rho_i$. The perturbed potential $\delta \Phi$ is set to zero at the radial boundaries. When a marker moves out of the radial boundary, its vertical location is changed from Z to $-Z$ (this is to follow the drift orbit) and its weight is set to zero, where Z is the vertical coordinate of cylindrical coordinates.

5.1 Linear results of ITG instabilities and benchmarking with other codes

Figure. 3 shows the time evolution of an $n = 29$ linear ITG instability for DIII-D cyclone base case parameters. Clear exponential growth of the instability is observed. The frequency and growth rate in this case are

$\omega_r/\Omega_i = 2.388 \times 10^{-3}$ and $\gamma/\Omega_i = 5.8 \times 10^{-4}$ while the corresponding results from Ref. [20] are $\omega_r/\Omega_i = 2.423 \times 10^{-3}$ and $\gamma/\Omega_i = 6.0 \times 10^{-4}$.
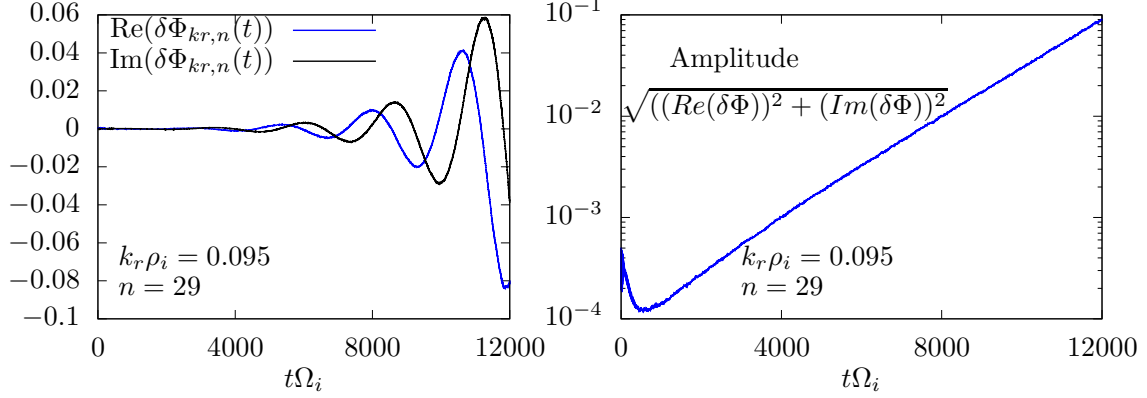

Figure 3. Time evolution of an $n=29$ linear ITG instability for DIII-D cyclone base case parameters. In the simulation, the perturbed electric potential $\delta\Phi$ is Fourier filtered along the toroidal direction to retain only the $n=29$ harmonic, which is further sine transformed along the radial direction and only low radial harmonics are retained. Shown here is the fundamental radial sine harmonic of $\delta\Phi$ near the low-field-side midplane, which corresponds to $k_r\rho_i = 0.095$. $\delta\Phi$ is normalized by T_e/e. The frequency and growth rate in this case are $\omega_r/\Omega_i = 2.388 \times 10^{-3}$ and $\gamma/\Omega_i = 5.8 \times 10^{-4}$, which correspond to the fifth data point in Fig. 6, where the corresponding results from Ref. [20] are $\omega_r/\Omega_i = 2.423 \times 10^{-3}$ and $\gamma/\Omega_i = 6.0 \times 10^{-4}$.

This is a multi-scale simulation, which includes both the slow-scale ITG instability and the fast-scale wave associated with the ion gyro-motion. In the simulation, we can identify the existence of the ion Bernstein wave (IBW) associated with the ion gyro-motion. The IBW is hidden in the simulation in Fig. 3, the details of which are plotted in Fig. 4(a) for $t\Omega_i = [0:200]$. The corresponding frequency spectrum is plotted in Fig 4(b), which shows a clear peak near the ion gyro-frequency.
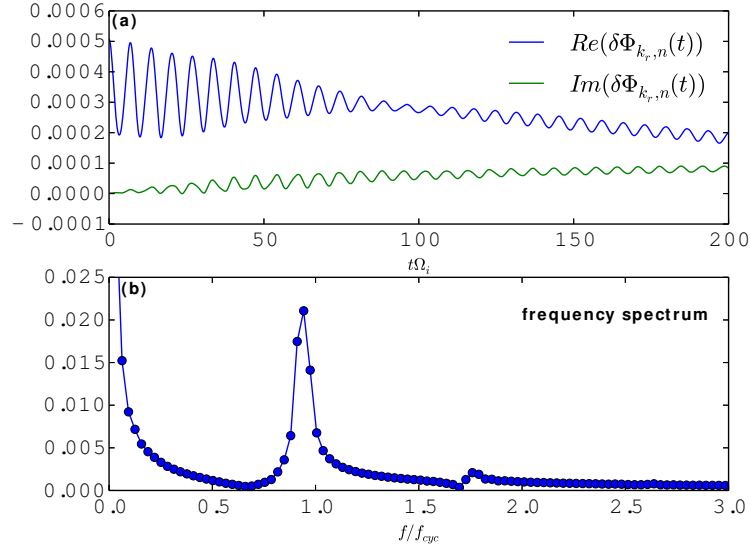

Figure 4. Time evolution (a) of the electric potential during $t\Omega_i = [0:200]$ and the corresponding frequency spectrum (b), which shows a clear peak near the ion gyro-frequency. Here $f_{\rm cyc} = \Omega_i/2\pi$.

Numerical parameters used in obtaining the above and the following results are as follows: the time step $\Delta t\Omega_i = 0.2$, the spatial resolution in (ψ, θ, α) is $(162, 64, 32)$, where the toroidal range is a wedge with $\Delta\alpha = 2\pi/n$, the number of total markers $N_p = 6.4 \times 10^6$ (the number of markers per cell is about 19).

Increasing the number of markers to $N_p = 9.6 \times 10^6$ produced no significant difference in the growth rate, as is shown in Fig. 5.
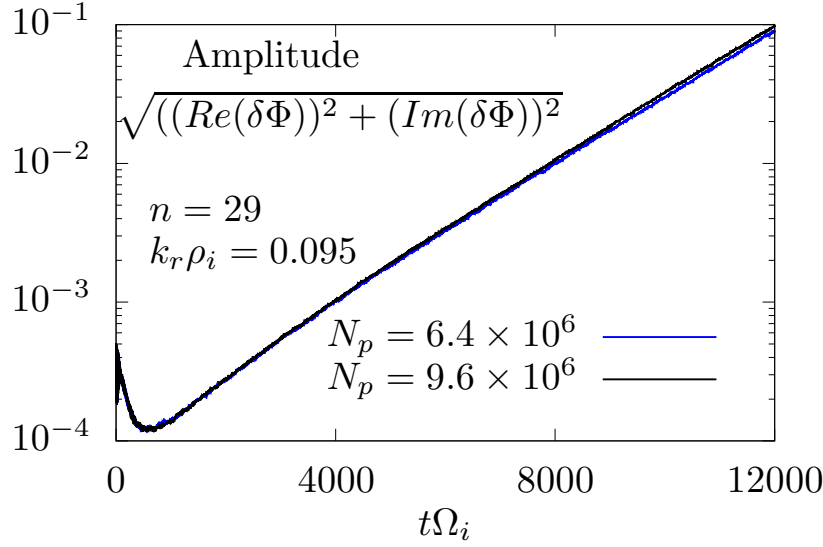

Figure 5. Comparison of ITG instabilities computed with different marker numbers $N_p = 6.4 \times 10^6$ and $N_p = 9.6 \times 10^6$. Other parameters are the same as those in Fig. 3.

The code uses one dimensional domain decomposition along θ and 4 MPI processes are used for particle parallelization for each θ cell and thus total $64 \times 4 = 256$ MPI processes are used. The code run on NERSC Cori system and typical runs use eight Intel Xeon "Haswell" nodes, each of which is equipped with 32 physical cores supporting 2 hyper-threads and thus $2 \times 32 = 64$ logical cores. The code uses OpenMP to make use of this hyper-threading capability. For the above run with 6×10^4 time-steps, the wall-time is 2.3 hours. (Each Cori node has two sockets and each socket is populated with a 16-core Intel® Xeon™ Processor E5-2698 v3 at 2.3 GHz.)

Figure 6 presents the dependence of the linear ITG mode frequency and growth rate on the ion temperature gradient κ_{T_i}, which shows that both the frequency and growth rate increase with the temperature gradient drive. Also plotted in Fig. 6 are the fully kinetic results from Ref. [20], which are in good agreement with our new results.
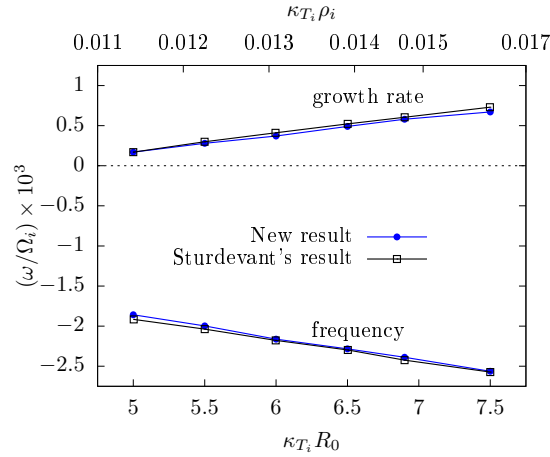

Figure 6. Dependence of ITG mode frequency and growth rate on the ion temperature gradient κ_{T_i} for the DIII-D cyclone base case. The upper horizontal axis shows the ion temperature gradient normalized by the thermal ion gyroradius. Also plotted are the results from Ref. [20], which are in good agreement with our new results.

Gyrokinetic simulations found that ITG instabilities usually reach a peak growth rate near a particular toroidal mode number n in the scanning over n due to the finite Larmor radius stabilizing effect. This trend can also be captured by the fully kinetic ion model. Figure 7 shows the dependence of ITG growth rate and frequency on toroidal mode number n, where the dependence on the poloidal wave-number k_θ defined by $k_\theta \approx n q_0 / r_0$ is also shown. Figure 7 shows that the growth rate reaches a peak near $k_\theta \rho_i \approx 0.4$. Also plotted in Fig. 7 are the gyrokinetic results from Ref. [22] and [21], which roughly agree with our results. The difference between our results and those from GENE 2010 (Ref. [22]) is mainly due to the difference in the value of the thermal ion gyro-radius at the magnetic axis ρ_i. In our simulation, $\rho_i = R_0/450.5$, while $\rho_i = R_0/500.0$ in Ref. [22]. Without redoing the simulation, we re-plot the results by using $k_\theta \rho_i$ consistent with that of GENE 2010, yielding the results in Fig. 8, which shows better agreement between our results and GENE 2010. Several other factors may also contribute to the difference between the three results. Safety factor profiles are slightly different: $q(r) = q_0 + (r - r_0)q'(r_0)$ in this work, while $q(r) = 0.86 - 0.16r/a + 2.52(r/a)^2$ in Ref. [22] and q profile variation is neglected in the flux-tube model of Ref. [21]. The radial variation of the density and temperature is neglected in the present work and Ref. [21] while Ref [22] includes the density and temperature profile.
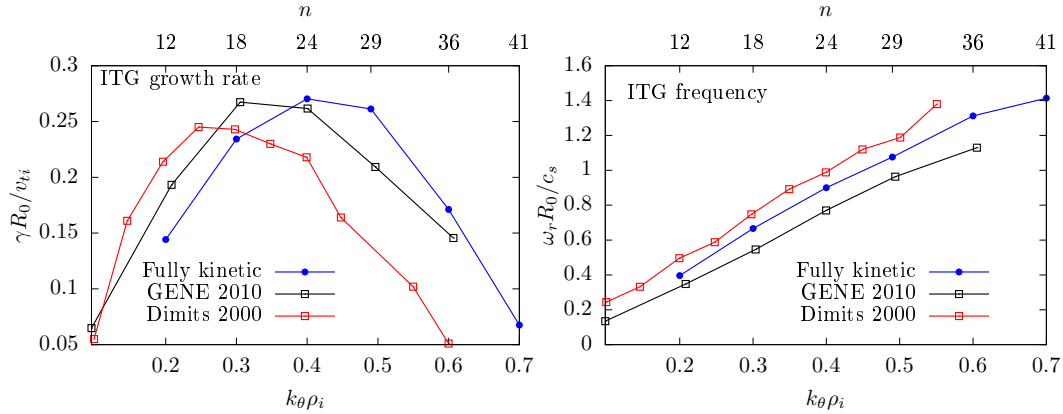

Figure 7. Dependence of ITG mode growth rate and frequency on $k_\theta \rho_i$ for DIII-D cyclone base case. The upper horizontal axis shows the corresponding toroidal mode number n. Also plotted are the gyrokinetic results reported in Ref. [22] and [21].
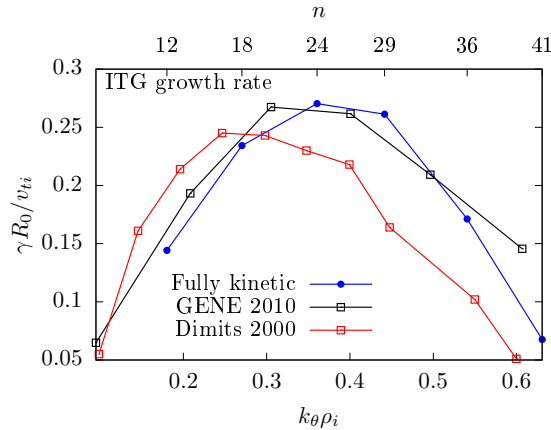

Figure 8. A re-plot of the results in Fig. 7. The only modification is that the value of $k_\theta \rho_i$ used in plotting the fully kinetic results is scaled by a factor of $450.5/500.0$ to take into account the different values of ρ_i used in the simulation. Compared with Fig. 7, the agreement between our results and GENE results is improved.

Figure 9 plots the two-dimensional mode structure of the $n = 29$ ITG instability in the poloidal plane, which shows a clear ballooning structure (i.e., the amplitude on the low-field-side is larger than that on the high-field-side). This is consistent with the physical picture that ITG instabilities are driven by the $E \times B$

drift on the tokamak low-field-side while the $E \times B$ drift on the high-field side (the "good-curvature" side) suppresses the instabilities.
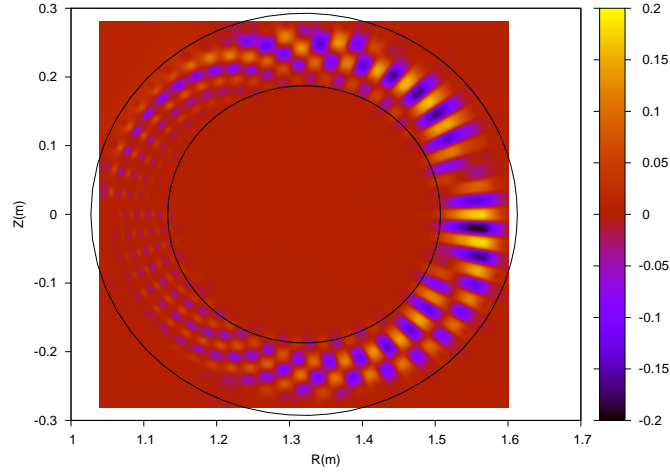

Figure 9. Mode structure of the $n = 29$ ITG instability in the poloidal plane. Plotted here is the perturbed electric potential $\delta\Phi$ at $t\Omega_i = 12000$.

5.2 Nonlinear results of ITG instabilities and analysis of saturation due to $E \times B$ trapping

With the Boris integrator, it is straightforward to extend the adiabatic electron model to the nonlinear regime, by including the electric field terms in the integration of particle trajectories. In a single-n simulation, the ITG instability saturates due to the $\mathbf{E} \times \mathbf{B}$ trapping, as discussed in Ref. [19] for slab geometry. Figure 10 plots the nonlinear evolution of the $n = 29$ ITG instability, along with the $\mathbf{E} \times \mathbf{B}$ trapping prediction for the saturation amplitude.
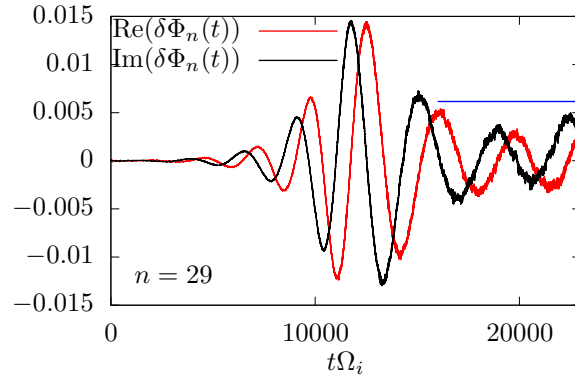

Figure 10. Nonlinear saturation of the $n = 29$ ITG instability in the DIII-D cyclone base case. The perturbed potential $\delta\Phi$ (normalized by T_e/e) is measured on the low-field-side midplane and averaged over the radial domain. The blue line shows the saturation predicted by the $E \times B$ trapping formula (26), which gives $e\delta\Phi_s/T_e = 6.16 \times 10^{-3}$ for this case.

The instability is expected to saturate when the $\mathbf{E} \times \mathbf{B}$ trapping angular frequency $\omega_{E \times B}$ becomes as large as the instability growth rate, i.e.,

$$\omega_{E \times B} \approx \gamma, \tag{21}$$

where $\omega_{E \times B}$ is proportional to the amplitude of $\delta\Phi$. The trapping frequency $\omega_{E \times B}$ can be estimated by calculating the time for a particle with the $\mathbf{E} \times \mathbf{B}$ drift velocity to go around the eddies of the potential $\delta\Phi$. The circumference l of the $\delta\Phi$ eddies in the poloidal plane can be estimated as the fundamental radial wavelength in the sine expansion, i.e., $l \approx \pi / k_r$. The $\delta\mathbf{E} \times \mathbf{B}_0$ drift is given by

$$\mathbf{V}_{E \times B} = \frac{\delta\mathbf{E} \times \mathbf{b}}{\mathbf{B}_0} = -\frac{\nabla\delta\Phi \times \mathbf{b}}{\mathbf{B}_0}, \tag{22}$$

which is along the contours of $\delta\Phi$. Using the poloidal wavenumber $k_\theta = n q_0 / r_0$ to estimate the gradient of $\delta\Phi$, then the magnitude of the $\delta\mathbf{E} \times \mathbf{B}_0$ drift can be estimated as

$$V_{E \times B} \approx \frac{\delta\Phi}{B_0} \frac{n q_0}{r_0}. \tag{23}$$

Then the $\delta\mathbf{E} \times \mathbf{B}_0$ trapping angular frequency can be written as

$$\omega_{E \times B} = \frac{2\pi}{T_{E \times B}} = \frac{2\pi V_{E \times B}}{l} \approx 2\frac{\delta\Phi}{B_0} \frac{n q_0}{r_0} k_r. \tag{24}$$

Using this expression, the saturation amplitude $\delta\Phi_s$ predicted by the critical condition (21) is written as

$$\delta\Phi_s \approx \gamma B_0 \frac{1}{2 k_r} \frac{r_0}{n q_0}. \tag{25}$$

Then the normalized potential $e\delta\Phi_s / T_e$ is written as

$$\frac{e}{T_e}\delta\Phi_s \approx \frac{\gamma}{\Omega_i} \frac{1}{2 k_r \rho_i} \frac{r_0 / \rho_i}{n q_0}. \tag{26}$$

Using $\gamma / \Omega_i = 5.8 \times 10^{-4}$, $k_r \rho_i = 0.095$, $r_0 / \rho_i = 81.9$, $n = 29$, and $q_0 = 1.4$, the above formula gives $e\delta\Phi_s / T_e = 6.16 \times 10^{-3}$. As is shown in Fig. (10), this estimation roughly agrees with the saturation amplitude observed in the simulation.

Physically, the dominant saturation mechanism of ITG instability is the nonlinear generation of an $n = 0$ zonal flow, which suppresses the ITG instability through radial shear. With fully kinetic ions, the adiabatic electron model gives no explicit equation for the $\delta\Phi$ with $n = 0$, making it difficult to solve the field equation, so we do not demonstrate that mechanism here. Extended models to capture this effect are the subject of ongoing investigation. Ref. [19] included the electron polarization response to model the $n = 0$ response. Another option is to use the ion momentum equation to indirectly enforce quasi-neutrality. These models are outside the scope of this work.

6 Summary

The viability of the fully kinetic ion model in simulating the low-frequency ITG instability in tokamaks is demonstrated in this work by using the toroidal Boris full orbit integrator. The equilibrium full orbits computed by this integrator conserve the kinetic energy accurate to the round-off error and the relative error in the toroidal angular momentum conservation is within 0.04% over a time period of $t\Omega_i = 2.5 \times 10^4$. This work extends the previous work to the nonlinear regime and investigates the nonlinear saturation of a single-n ITG instability due to the $E \times B$ trapping mechanism. The saturation amplitude predicted by the $E \times B$ trapping is found to agree with the saturation level observed in the simulation. This work also extends the previous work from analytic circular magnetic equilibria to general magnetic equilibria, enabling simulation of realistic equilibria reconstructed from tokamak experiments.

This work is limited to the electrostatic case with the simple adiabatic electron model. The nonlinear case reported in this paper is limited to the saturation of a single-n mode. Future work will consider electromagnetic effects using more accurate drift-kinetic model for electrons. The nonlinear case will be extended to include interactions between ITG modes of multiple toroidal mode numbers and their coupling to the zonal flow.

The Fortran code used in obtaining the results presented in this work is released as an open-source software under the GNU General Public License v3.0. The source code can be downloaded from: https://github.com/Youjunhu/Fully_kinetics_tokamak_ITG.

Acknowledgments

Bibliography

[1] P. N. Guzdar, L. Chen, W. M. Tang, and P. H. Rutherford, The Physics of Fluids **26**, 673 (1983).

[2] C. L. Rettig, T. L. Rhodes, J. N. Leboeuf, W. A. Peebles, E. J. Doyle, G. M. Staebler, K. H. Burrell, and R. A. Moyer, Physics of Plasmas **8**, 2232 (2001).

[3] Z. Lin, T. S. Hahm, W. W. Lee, W. M. Tang, and R. B. White, Science **281**, 1835 (1998).

[4] H. S. Xie, Y. Xiao, and Z. Lin, Phys. Rev. Lett. **118**, 095001 (2017).

[5] S. E. Parker, W. W. Lee, and R. A. Santoro, Phys. Rev. Lett. **71**, 2042 (1993).

[6] Y. Idomura, S. Tokuda, and Y. Kishimoto, Nuclear Fusion **43**, 234 (2003).

[7] Z. Gao, H. Sanuki, K. Itoh, and J. Q. Dong, Physics of Plasmas **12**, 022502 (2005).

[8] Y. Chen and S. E. Parker, Journal of Computational Physics **220**, 839 (2007).

[9] L. Ye, Y. Xu, X. Xiao, Z. Dai, and S. Wang, Journal of Computational Physics **316**, 180 (2016).

[10] T. Görler, X. Lapillonne, S. Brunner, T. Dannert, F. Jenko, F. Merz, and D. Told, Journal of Computational Physics **230**, 7053 (2011).

[11] S. Ku, C. Chang, and P. Diamond, Nuclear Fusion **49**, 115021 (2009).

[12] C. S. Chang, S. Ku, G. R. Tynan, R. Hager, R. M. Churchill, I. Cziegler, M. Greenwald, A. E. Hubbard, and J. W. Hughes, Phys. Rev. Lett. **118**, 175001 (2017).

[13] E. V. Belova, N. N. Gorelenkov, and C. Z. Cheng, Physics of Plasmas **10**, 3240 (2003).

[14] Y. Lin, X. Y. Wang, L. Chen, X. Lu, and W. Kong, Plasma Physics and Controlled Fusion **53**, 054013 (2011).

[15] R. E. Waltz and Z. Deng, Physics of Plasmas **20**, 012507 (2013).

[16] G. J. Kramer, R. V. Budny, A. Bortolon, E. D. Fredrickson, G. Y. Fu, W. W. Heidbrink, R. Nazikian, E. Valeo, and M. A. V. Zeeland, Plasma Physics and Controlled Fusion **55**, 025013 (2013).

[17] A. Kuley, Z. Lin, J. Bao, X. S. Wei, Y. Xiao, W. Zhang, G. Y. Sun, and N. J. Fisch, Physics of Plasmas **22**, 102515 (2015).

[18] B. J. Sturdevant, S. E. Parker, Y. Chen, and B. B. Hause, Journal of Computational Physics **316**, 519 (2016).

[19] M. T. Miecnikowski, B. J. Sturdevant, Y. Chen, and S. E. Parker, Physics of Plasmas **25**, 055901 (2018).

[20] B. J. Sturdevant, Y. Chen, and S. E. Parker, Physics of Plasmas **24**, 081207 (2017).

[21] A. M. Dimits, G. Bateman, M. A. Beer, B. I. Cohen, W. Dorland, G. W. Hammett, C. Kim, J. E. Kinsey, M. Kotschenreuther, A. H. Kritz, L. L. Lao, J. Mandrekas, W. M. Nevins, S. E. Parker, A. J. Redd, D. E. Shumaker, R. Sydora, and J. Weiland, Physics of Plasmas **7**, 969 (2000).

[22] X. Lapillonne, B. F. McMillan, T. Görler, S. Brunner, T. Dannert, F. Jenko, F. Merz, and L. Villard, Physics of Plasmas **17**, 112321 (2010).

[23] C. Birdsall and A. Langdon, *Plasma Physics via Computer Simulation*, CRC Press, 2004.

[24] S. E. Parker and W. W. Lee, Physics of Fluids B: Plasma Physics **5**, 77 (1993).

[25] A. Y. Aydemir, Physics of Plasmas **1**, 822 (1994).

[26] E. Süli and D. F. Mayers, *An Introduction to Numerical Analysis*, Cambridge University Press, 2003.

[27] H. Qin, S. Zhang, J. Xiao, J. Liu, Y. Sun, and W. M. Tang, Physics of Plasmas **20**, 084503 (2013).

[28] S. Parker and C. Birdsall, Journal of Computational Physics **97**, 91 (1991).

[29] L. Lao, H. S. John, R. Stambaugh, A. Kellman, and W. Pfeiffer, Nucl. Fusion **25**, 1611 (1985).

[30] M. A. Beer, S. C. Cowley, and G. W. Hammett, Phys. Plasmas (1994-present) **2**, 2687 (1995).

[31] Y. Chen and S. E. Parker, Journal of Computational Physics **189**, 463 (2003).